The Astrophysical Journal, 923:22 (16pp), 2021 December 10 https://doi.org/10.3847/1538-4357/ac282c

Spectroscopy and Photometry of the Least Massive Type II Globular Clusters: NGC 1261 and NGC 6934*

A. F. Marino[1], A. P. Milone[2,3], A. Renzini[3], D. Yong[4], M. Asplund[5], G. S. Da Costa[4], H. Jerjen[4], G. Cordoni[2], M. Carlos[2], E. Dondoglio[2], E. P. Lagioia[2], S. Jang[2], and M. Tailo[2]

[1] Istituto Nazionale di Astrofisica—Osservatorio Astrofisico di Arcetri, Largo Enrico Fermi, 5, I-50125 Firenze, Italy; anna.marino@inaf.it
[2] Dipartimento di Fisica e Astronomia "Galileo Galilei," Università di Padova, Vicolo dell'Osservatorio 3, I-35122 Padua, Italy
[3] Istituto Nazionale di Astrofisica—Osservatorio Astronomico di Padova, Vicolo dell'Osservatorio 5, I-35122 Padua, Italy
[4] Research School of Astronomy & Astrophysics, Australian National University, Canberra, ACT 2611, Australia
[5] Max Planck Institute for Astrophysics, Karl-Schwarzschild-Str. 1, D-85741 Garching, Germany
Received 2021 June 30; revised 2021 September 11; accepted 2021 September 18; published 2021 December 8

Abstract

Recent work has revealed two classes of globular clusters (GCs), dubbed Type I and Type II. Type II GCs are characterized by both a blue and a red red giant branch composed of stars with different metallicities, often coupled with distinct abundances in the slow neutron-capture elements (s-elements). Here we continue the chemical tagging of Type II GCs by adding the two least massive clusters of this class, NGC 1261 and NGC 6934. Based on both spectroscopy and photometry, we find red stars in NGC 1261 to be slightly enhanced in [Fe/H] by ∼0.1 dex and confirm that red stars of NGC 6934 are enhanced in iron by ∼0.2 dex. Neither NGC 1261 nor NGC 6934 show internal variations in the s-elements, which suggests a GC mass threshold for the occurrence of *s*-process enrichment. We found a significant correlation between the additional Fe locked in the red stars of Type II GCs and the present-day mass of the cluster. Nevertheless, most Type II GCs retained a small fraction of Fe produced by SNe II, lower than the 2%; NGC 6273, M54, and ω Centauri are remarkable exceptions. In the Appendix, we infer for the first time chemical abundances of lanthanum, assumed as representative of the s-elements, in M54, the GC located in the nucleus of the Sagittarius dwarf galaxy. Red-sequence stars are marginally enhanced in [La/Fe] by 0.10 ± 0.06 dex, in contrast with the large [La/Fe] spread of most Type II GCs. We suggest that different processes are responsible for the enrichment in iron and *s*-elements in Type II GCs.

Unified Astronomy Thesaurus concepts: Globular star clusters (656); Population II stars (1284); Chemical abundances (224); CCD photometry (208); Hertzsprung Russell diagram (725)

1. Introduction

Based on data collected through the Hubble Space Telescope (HST) photometric survey of Milky Way globular clusters (GCs), we have established a powerful photometric diagram to investigate multiple stellar populations, i.e., a combination of four HST bands (F275W, F336W, F438W, and F814W) allowing the construction of multiple color plots now nicknamed *Chromosome Maps* (ChM, Milone et al. 2015, 2017). The position of stars in these diagrams is especially sensitive to the abundance of C, N, and O elements via the molecules that they form (e.g., Marino et al. 2008) as well as to helium and the overall metallicity (Milone et al. 2015; Marino et al. 2019a). One of the most exciting discoveries from ChM analysis is that two different classes of GCs are hosted in the Milky Way. A first class includes the majority of GCs with their variations in the elements involved in hot H burning, with the typical Na–O, C–N, and sometimes Mg–Al, anticorrelations and homogeneous abundances in heavy elements. The ChM of these clusters is populated by two main stellar groups: (1) one corresponding to the O-enhanced population, also displaying normal Na, N, and He for their metallicity (hereafter 1P), and (2) the other one being depleted in O and C and enhanced in Na, N, and He (hereafter 2P) (Milone et al. 2015; Marino et al. 2019a). We usually refer to this class of objects as Type I GCs.

The second class of globular cluster represents ∼17% of the GCs analyzed in the HST survey. Their most distinctive feature is the presence of "more than one sequence" on the ChM. In addition to the ChM sequence made of 1P and 2P stars, common to all Milky Way GCs, this class displays an additional ChM sequence running on the red side of the main map.

Many of these objects have been spectroscopically classified as *anomalous* GCs, at odds with a typical cluster, host-stellar populations with different metallicities (*Z*) and, often, different abundances in the neutron-capture elements produced via slow neutron-capture reactions (*s*-elements, e.g., Yong & Grundahl 2008; Marino et al. 2009, 2011b, 2015; Yong et al. 2014; Johnson et al. 2015, 2017). Metallicity variations are associated with variations in [Fe/H], variations in the overall C+N+O abundance, or both (e.g., Yong et al. 2009; Marino et al. 2012a).

The color–magnitude diagrams (CMDs) of these clusters show multiple sub-giant branches (SGBs, Milone et al. 2008; Marino et al. 2012b) and red giant branches (RGBs, Marino et al. 2015, 2019a). Stars on the red RGB also define distinct sequences along the asymptotic giant branch and the horizontal branch (e.g., Dondoglio et al. 2021; Lagioia et al. 2021b). We dubbed this newly discovered class of objects Type II GCs.

The interest in Type II GCs comes from the fact that variations in the overall metallicity were considered a characteristic of more massive stellar systems such as galaxies, capable of retaining supernovae ejecta in contrast to ordinary GCs. In this context, ω Centauri, with its major internal

* Based on observations collected at the European Southern Observatory under ESO program 0101.D-0109(A), and the NASA/ESA Hubble Space Telescope, obtained at the Space Telescope Science Institute, which is operated by AURA, Inc., under NASA contract NAS 5-26555.

variations in metals, has always been considered the surviving nucleus of a disrupted dwarf galaxy (e.g., Bekki & Freeman 2003). Evidence of tidal debris from this massive GC reinforces the hypothesis that ω Centauri is indeed a dwarf galaxy remnant (Majewski et al. 2012; Ibata et al. 2019). However, it may well be that most GCs formed inside dwarfs, most of which later dissolved due to interactions within the growing Milky Way. Indeed, it is now widely accepted that many GCs are associated with stellar streams (e.g., Massari et al. 2019) and that half of the known Type II GCs appear clustered in a distinct region of the integral of motions space, thus suggesting a common progenitor galaxy (Milone et al. 2020).

Beside having internal variations in Fe, ω Centauri displays a clear enhancement in *s*-elements as metallicity increases (e.g., Norris & Da Costa 1995; Johnson & Pilachowski 2010; Marino et al. 2011a), making the similarity in the chemical pattern with the *anomalous* GCs remarkable (Da Costa & Marino 2011; Marino et al. 2015). Noticeably, one Type II GC, NGC 6715 (M54), lies in the central region of the Sagittarius dwarf galaxy (Bellazzini et al. 2008) and two others, NGC 1851 (Olszewski et al. 2009; Kuzma et al. 2018) and M2 (Kuzma et al. 2016), are surrounded by extended envelopes. The stellar halo surrounding NGC 1851 has a chemistry compatible with a galaxy remnant (Marino et al. 2014).

As previously discussed, the ChM of all the known *anomalous* GCs, e.g., those with metallicity variations, can be classified as a Type II map, with the Fe-richer stars populating the red additional patterns on the map (see Marino et al. 2019a). We are conducting chemical tagging, based on high-resolution spectroscopy, to infer the occurrence and size of the chemical abundance variations in the known Type II GCs. So far, we have chemical abundances measured on both the blue and red sequence of the ChM for eight Type II GCs. In the present work, we analyze chemical abundances of two among the less massive Type II GCs known so far, namely NGC 1261 and NGC 6934 (Milone et al. 2017). NGC 1261 has never been analyzed in the context of the link between the Type II morphology of the ChM and internal variations in heavy elements. Indeed, as discussed in Milone et al. (2017), the stars distributing on the additional redder sequence provide a minor contribution to the GC mass, and only ChM-guided spectroscopic campaigns can pinpoint them. Kuzma et al. (2018) recently found a stellar envelope surrounding this GC, suggesting that it might be the product of dynamical evolution of the cluster. Indeed, this stellar structure has a much smaller size than that observed around NGC 1851.

By contrast, four giants along the ChM of NGC 6934, two on the typical blue sequence and two others on the redder one, have already been analyzed by Marino et al. (2018). They found that the two redder stars have higher Fe abundances by $\sim$0.15 dex with respect to the other two stars, making this Type II GC a chemically *anomalous* GC. However, in contrast with the known Type II GCs, the two red stars do not show any evidence of enhancements in the *s*-elements. This difference may indicate a different chemical evolution of NGC 6934 with respect to the bulk of the *anomalous* GCs. Nevertheless, given the small sample size of Marino et al. (2018), the presence of *s*-enriched stars cannot be definitively ruled out.

The outline of the paper is as follows: Section 2 is a description of the spectroscopic and photometric data sets and the choice of adopted atmospheric parameters is discussed in Section 3, while our chemical abundance analysis is outlined in Section 4. Sections 5 and 6 describe the results for NGC 6934 and NGC 1261, respectively. Finally, all our results are summarized and discussed in Section 7.

Although M54 is providing perhaps the clearest evidence for a possible link between *anomalous* GCs and nuclei of dwarf galaxies, as far as we know, there is no analysis of *s*-element abundances in the stars with different Fe in this context. In the Appendix, we have filled this gap by measuring the first chemical abundances of lanthanum in giant stars whose spectra were analyzed by Carretta et al. (2010a). Our aim is to investigate if, similarly to other Type II GCs, these stars show internal variations in those species belonging to the neutron-capture element group.

2. Data

2.1. The Photometric Data Set: The Chromosome Map of NGC 1261 and NGC 6934

Photometric data used in this study come from the HST UV Legacy Survey to investigate multiple stellar populations in GCs (GO-13297, Piotto et al. 2015). Details on the images analyzed and data reduction can be found in Piotto et al. (2015) and Milone et al. (2017).

Milone et al. (2017) analyzed the ChMs of 57 GCs, including NGC 1261 and NGC 6934, and noticed some peculiarities (see their Figure 4) with respect to typical GC maps. The ChM of red giants in both clusters is reproduced in Figure 1 (left panels) where we can clearly distinguish: (i) the presence of 1P and 2P stars, as the stars located at lower and higher $\Delta_{\rm CF275W,F336W,F438W}$ values and (ii) two distinct sequences of stars represented with gray and red dots, respectively. As discussed in Section 1, the presence of the separate distribution of red stars on the ChM is a distinctive feature of the Type II GCs.

In the right panels of Figure 1 we show the $m_{\rm F336W}$ versus $m_{\rm F336W} - m_{\rm F814W}$ CMDs of the two analyzed clusters. Actually, the distinction between blue and red-RGB stars in Type II GCs can be made on *classical* CMDs (see Section 5 in Milone et al. 2017) either by using the $m_{\rm F336W}$ versus $m_{\rm F336W} - m_{\rm F814W}$ CMD based on HST filters or the U versus $U - I$ CMD from ground-based photometry (Marino et al. 2019a). Then, the blue and red RGBs are generally observed to define two distinct ChM sequences. Among our spectroscopic targets, we note just one star in NGC 1261 (#15), observed with UVES and classified as blue RGB on the CMD, but located in a position consistent with redder stars on the ChM (see Figure 1). In the following, this star is treated as a blue-RGB star, consistent with its location on the $m_{\rm F336W}$ versus $m_{\rm F336W} - m_{\rm F814W}$ CMD.

2.2. The Spectroscopic Data Set

Spectroscopic data for NGC 1261 and NGC 6934 have been acquired using the FLAMES Ultraviolet and Visual Echelle Spectrograph (FLAMES-UVES, Pasquini et al. 2000) on the European Southern Observatory (ESO) Very Large Telescope, through the program 0101.D-0109(A). The observations were taken in the standard RED580 setup, which has a wavelength coverage of 4726–6835 Å and a resolution $R \sim 47{,}000$ (Dekker et al. 2000). Together with the UVES fibers, we used GIRAFFE fibers with the HR13 setup to observe a sample of

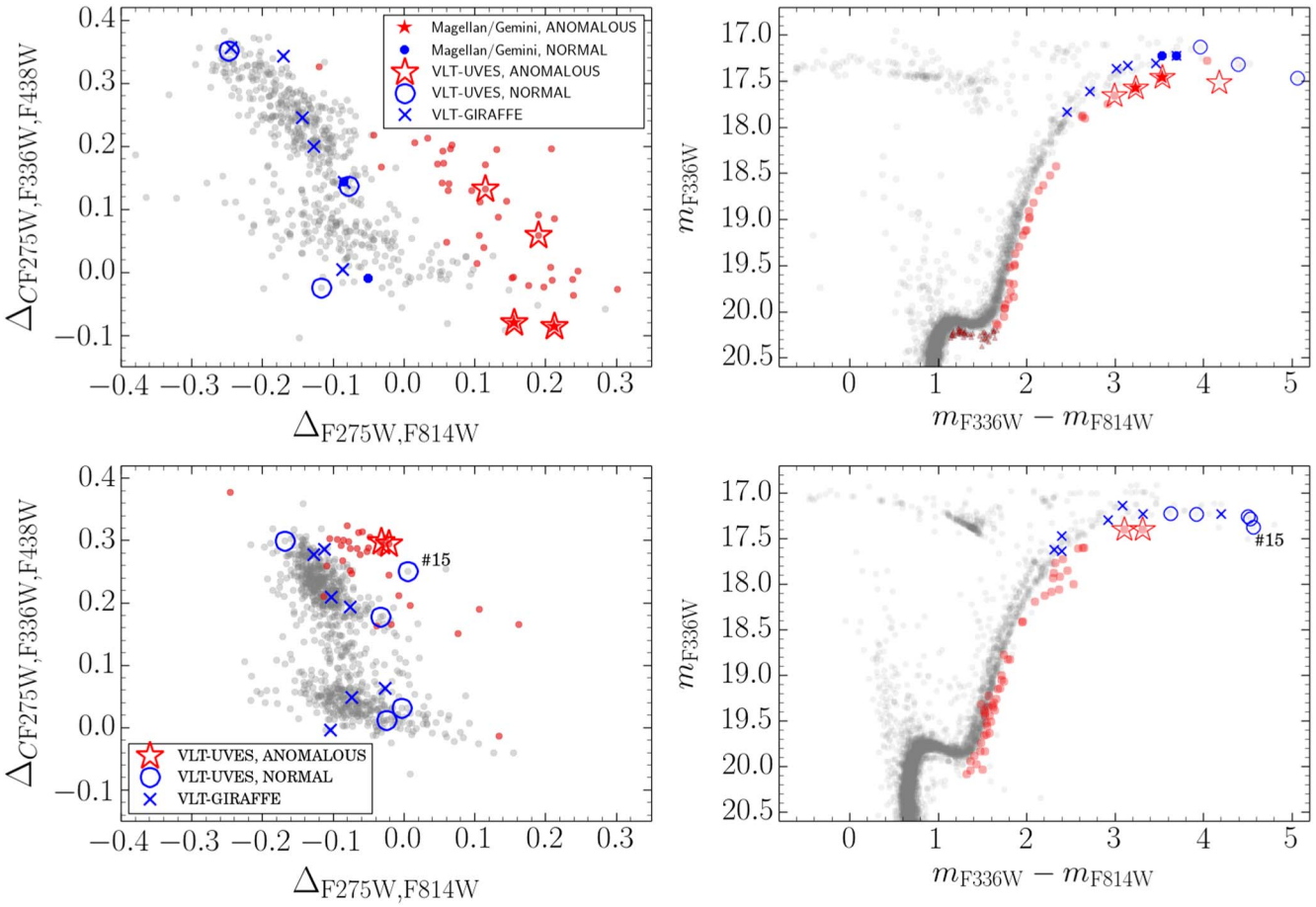

Figure 1. Chromosome maps (left panels) and m_{F336W} vs. $m_{F336W} - m_{F814W}$ CMDs (right panels) of the GCs NGC 6934 (upper panels) and NGC 1261 (lower panels). The stars colored in red have been selected as the stars defining the redder RGB stars on the CMDs. Open circles and star-like symbols represent blue and red RGB stars, respectively, observed with UVES; crosses are the GIRAFFE targets, all classified as blue-RGB stars. For NGC 6934 we also show stars observed with Magellan or the Gemini telescope from Marino et al. (2019a).

RGBs in the spectral range from ∼6122 to ∼6402 Å at a resolving power $R \sim 22{,}000$.

Spectra are based on 9 × 2775 s exposures for NGC 6934, and 7 × 2775 s exposures for NGC 1261. Observation details are provided in Table 1. UVES targets have been selected to be distributed on both the blue and red sequences of the CMD and the ChM (see previous section). For NGC 6934 we have observed three blue RGBs and four red RGBs (two of which were also observed in Marino et al. 2019a); our sample for NGC 1261 is composed of four blue and two red RGBs.

Data were reduced using the ESO pipelines for FLAMES within the EsoReflex interface[6] (Ballester et al. 2000), including bias subtraction, flat-field correction, wavelength calibration, sky subtraction, and spectral rectification. Once individual spectra were reduced, the telluric subtraction has been performed by using the ESO MOLECFIT tool (Kausch et al. 2014; Smette et al. 2015). Co-addition of the individual exposures, continuum normalization, and correction to laboratory wavelength was performed using IRAF routines.

Radial velocities (RVs) were derived using the IRAF@FXCOR task, which cross correlates the object spectrum with a template. For the template we used a synthetic spectrum generated with the latest version of MOOG[7] (version 2014 June, Sneden 1973). This spectrum was computed with a model stellar atmosphere interpolated from the Castelli & Kurucz (2004) grid, adopting parameters (effective temperature ($T_{\rm eff}$), surface gravity ($\log g$), microturbulence ($\xi_{\rm t}$), metallicity ([A/H])) of 4600 K, 2.5, 2.0 km s^{-1}, and −1.45 dex, respectively. Observed RVs were then corrected to the heliocentric system.

Heliocentric RVs were used to establish cluster membership for our targets. In the end, our sample of stars on the ChM is composed of 13 red giant stars in NGC 6934 and 14 in NGC 1261 (both GIRAFFE and UVES). For the two clusters we measure average RVs of $\langle {\rm RV} \rangle = -408.6 \pm 1.2$ km s^{-1} (rms = 4.2 km s^{-1}), and $\langle {\rm RV} \rangle = +71.1 \pm 1.1$ km s^{-1} (rms = 3.8 km s^{-1}), for NGC 6934 and NGC 1261, respectively. These values are in good agreement with those reported in the 2010 version of the Harris (1996) catalog (−411.4 ± 1.6 and 68.2 ± 4.6 for NGC 6934 and NGC 1261, respectively).

3. Model Atmospheres

First estimates of the atmospheric parameters for the program stars have been derived by taking advantage of our photometry, from both HST and ground-based facilities. The m_{F606W} and m_{F814W} mag from HST have been converted to V and I (Anderson et al. 2008), which we then used to estimate effective temperatures from the color-temperature calibrations (Alonso et al. 1999), assuming mean reddening values of $E(B-V) = 0.10$ and $E(B-V) = 0.01$ for NGC 6934 and

[6] https://www.eso.org/sci/software/esoreflex/
[7] http://www.as.utexas.edu/chris/moog.html

Table 1
Observation Details: Coordinates, Radial Velocities, with Associated rms, and Number of Exposures for Our Spectroscopic Targets Observed with UVES and GIRAFFE

GC	Star	R.A. J2000	Decl. J2000	RV_{helio} (km s^{-1})	rms (km s^{-1})	# Exposures	Source	Alternative ID (Marino et al. 2019a)
NGC 6934	37	20:34:12.28	07:24:16.3	–409.74 ±0.05	0.19	9	UVES	
NGC 6934	29	20:34:14.37	07:24:49.3	–414.88 ±0.03	0.14	9	UVES	
NGC 6934	27	20:34:16.46	07:24:53.3	–402.72 ±0.06	0.23	9	UVES	NGC 6934-a1
NGC 6934	14	20:34:13.66	07:24:07.2	–414.85 ±0.14	0.57	9	UVES	
NGC 6934	1	20:34:13.80	07:22:47.8	–408.36 ±0.05	0.22	9	UVES	
NGC 6934	5	20:34:10.34	07:23:21.2	–412.25 ±0.08	0.35	9	UVES	
NGC 6934	47	20:34:07.58	07:24:17.1	–402.50 ±0.06	0.26	9	UVES	NGC 6934-a2
NGC 6934	22	20:34:09.77	07:24:09.5	–411.52 ±0.05	0.15	9	GIRAFFE	
NGC 6934	23	20:34:09.72	07:23:27.5	–407.54 ±0.04	0.13	9	GIRAFFE	
NGC 6934	34	20:34:12.63	07:24:40.4	–405.94 ±0.09	0.27	9	GIRAFFE	
NGC 6934	35	20:34:12.63	07:24:57.1	–407.24 ±0.05	0.15	9	GIRAFFE	
NGC 6934	42	20:34:10.39	07:24:17.8	–411.15 ±0.04	0.11	9	GIRAFFE	NGC 6934-n1
NGC 6934	50	20:34:11.89	07:25:26.7	–403.68 ±0.12	0.35	9	GIRAFFE	
NGC 1261	14	03:12:19.83	−55:13:08.0	65.89 ±0.09	0.34	7	UVES	
NGC 1261	15	03:12:19.60	−55:13:42.6	72.61 ±0.41	1.49	7	UVES	
NGC 1261	17	03:12:18.25	−55:13:31.0	76.49 ±0.10	0.35	7	UVES	
NGC 1261	36	03:12:21.40	−55:12:24.5	75.62 ±0.12	0.42	7	UVES	
NGC 1261	49	03:12:15.44	−55:12:21.3	67.07 ±0.07	0.24	7	UVES	
NGC 1261	52	03:12:09.78	−55:12:49.9	65.28 ±0.06	0.22	7	UVES	
NGC 1261	6	03:12:12.87	−55:13:52.1	72.20 ±0.15	0.55	7	UVES	
NGC 1261	7	03:12:10.53	−55:14:07.4	74.52 ±0.16	0.39	7	GIRAFFE	
NGC 1261	22	03:12:14.88	−55:13:40.4	74.38 ±0.10	0.24	7	GIRAFFE	
NGC 1261	24	03:12:13.62	−55:13:24.8	74.24 ±0.16	0.38	7	GIRAFFE	
NGC 1261	35	03:12:25.58	−55:12:53.3	69.79 ±0.10	0.25	7	GIRAFFE	
NGC 1261	40	03:12:19.31	−55:12:33.3	66.57 ±0.10	0.24	7	GIRAFFE	
NGC 1261	54	03:12:22.86	−55:12:04.4	69.82 ±0.09	0.23	7	GIRAFFE	
NGC 1261	61	03:12:13.49	−55:11:47.7	70.60 ±0.08	0.19	7	GIRAFFE	

NGC 1261, respectively (Harris 2010). Surface gravities were then obtained from the V magnitudes, the photometric temperatures, bolometric corrections from Alonso et al. (1999), distance modulus of $(m-M)_V = 16.28$ for NGC 6934 and $(m-M)_V = 16.09$ for NGC 1261 (Harris 2010). The stellar mass has been fixed to $0.70\,M_{\odot}$. Photometric temperatures and surface gravities are listed in Table 2.

The high resolution and the large spectral coverage of the UVES spectra allowed us to have a fully spectroscopic estimate of $T_{\rm eff}$ and $\log g$ from Fe lines. Hence, we determined $T_{\rm eff}$ by imposing the excitation potential (E.P.) equilibrium of the Fe I lines and gravity with the ionization equilibrium between Fe I and Fe II lines. Note that for $\log g$ we impose Fe II abundances that are 0.06–0.08 dex higher than the Fe I ones to adjust for non-local thermodynamic equilibrium (non-LTE) effects (Bergemann et al. 2012; Lind et al. 2012; Amarsi et al. 2016). The microturbulent velocity was set to minimize any dependence on Fe I abundances as a function of equivalent widths (EWs). Spectroscopic parameters for stars observed with UVES are listed in Table 2.

By comparing the spectroscopic and photometric $T_{\rm eff}/\log g$ obtained from the UVES spectra for NGC 6934, we notice that spectroscopic $T_{\rm eff}$ values are higher by $+52 \pm 8$ K (rms = 20 K). Surface gravities are on the same scale with average differences $\Delta\log g = \log g_{(V-I)} - \log g_{\rm Fe\ lines} = -0.05 \pm 0.05$ (rms = 0.12). Similar offsets have been obtained for NGC 1261, for which we get spectroscopic $T_{\rm eff}$ higher by $+36 \pm 9$ K (rms = 22 K), and $\Delta\log g = \log g_{(V-I)} - \log g_{\rm Felines} = -0.01 \pm 0.03$ (rms =0.07). This comparison suggests that internal estimates of uncertainties associated with our atmospheric parameters are ∼50 K for $T_{\rm eff}$, and ∼0.15 dex for $\log g$. For ξ_t and metallicity we adopt typical internal uncertainties of 0.20 km s^{-1} and 0.10 dex, respectively.

For GIRAFFE spectra, once temperatures and gravities were fixed from photometry, we derived metallicities and microturbulences from the Fe I lines as explained above. As a comparison, Table 2 also lists the ξ_t values from the ξ_t–$\log g$ empirical relation obtained by Marino et al. (2008). For the GIRAFFE targets we assume the same uncertainties associated with the stellar parameters that we used for UVES.

4. Chemical Abundance Analysis

Chemical abundances were derived from a local thermodynamic equilibrium (LTE) analysis by using the spectral analysis code MOOG (Sneden 1973), and the alpha-enhanced Kurucz model atmospheres of Castelli & Kurucz (2004), whose parameters have been obtained as described in Section 3.

For UVES spectra we infer chemical abundances for proton-capture elements O, Na, Mg, and Al; for α elements Si, Ca, Ti (I and II), Sc (II), V, Cr (I and II), Mn, Fe (I and II), Co, Ni, Cu, and Zn; and neutron-capture elements Y (II), Zr (II), Ba (II), La (II), Ce (II), Pr (II), Nd (II), and Eu (II). The chemical abundances for all the elements, with the exceptions of O, Al, Mn, Cu, Zr, Ba, La, Ce, Pr, and Eu, for which spectral synthesis has been employed, have been inferred from an EW-based analysis. A detailed description of all the spectral features analyzed from UVES and GIRAFFE data can be found

Table 2
Atmospheric Parameters for Our Spectroscopic Targets Observed with UVES and GIRAFFE

GC	Star	$T_{\rm eff}$	log g	[Fe/H]	$\xi_{\rm t}$	$T_{\rm eff\,phot}$	log g	$\xi_{\rm t}$	Source
NGC 6934	37	4280	1.03	−1.36	1.55	4214	0.90	1.70	UVES
NGC 6934	29	4620	1.72	−1.34	1.45	4580	1.59	1.52	UVES
NGC 6934	27	4490	1.50	−1.30	1.51	4453	1.41	1.57	UVES
NGC 6934	14	4350	0.70	−1.60	2.05	4279	0.87	1.71	UVES
NGC 6934	1	4240	0.90	−1.53	1.90	4165	0.72	1.75	UVES
NGC 6934	5	4050	0.43	−1.52	2.20	4029	0.42	1.82	UVES
NGC 6934	47	4430	1.23	−1.35	1.63	4379	1.22	1.62	UVES
NGC 6934	22	4545	1.46	−1.62	1.22	4545	1.46	1.56	GIRAFFE
NGC 6934	23	4485	1.37	−1.64	1.50	4485	1.37	1.58	GIRAFFE
NGC 6934	34	4644	1.71	−1.69	1.33	4644	1.71	1.50	GIRAFFE
NGC 6934	35	4432	1.20	−1.56	1.60	4432	1.20	1.62	GIRAFFE
NGC 6934	42	4342	1.05	−1.58	1.67	4342	1.05	1.66	GIRAFFE
NGC 6934	50	4735	1.92	−1.61	1.08	4735	1.92	1.44	GIRAFFE
NGC 1261	14	4400	1.15	−1.26	1.68	4337	1.13	1.64	UVES
NGC 1261	15	4150	0.70	−1.31	1.90	4107	0.71	1.75	UVES
NGC 1261	17	4470	1.40	−1.22	1.62	4469	1.38	1.58	UVES
NGC 1261	36	4300	1.05	−1.28	1.80	4255	0.98	1.68	UVES
NGC 1261	49	4120	0.60	−1.33	1.95	4106	0.69	1.76	UVES
NGC 1261	52	4570	1.60	−1.21	1.61	4521	1.49	1.55	UVES
NGC 1261	6	4130	0.60	−1.32	1.93	4094	0.68	1.76	UVES
NGC 1261	7	4738	2.03	−1.38	1.32	4738	2.03	1.41	GIRAFFE
NGC 1261	22	4544	1.59	−1.38	1.59	4544	1.59	1.53	GIRAFFE
NGC 1261	24	4185	0.89	−1.31	1.82	4185	0.89	1.70	GIRAFFE
NGC 1261	35	4691	1.92	−1.41	1.32	4691	1.92	1.44	GIRAFFE
NGC 1261	40	4411	1.35	−1.30	1.64	4411	1.35	1.59	GIRAFFE
NGC 1261	54	4720	2.00	−1.32	1.17	4720	2.00	1.42	GIRAFFE
NGC 1261	61	4460	1.42	−1.32	1.53	4460	1.42	1.57	GIRAFFE

in Marino et al. (2015, 2019b). The LTE approach is justified by the fact that we are mostly interested in abundance differences among different populations of stars with similar stellar parameters. Indeed, relative non-LTE abundance corrections are expected to be negligible for our purposes.

The chemical abundances obtained with UVES and GIRAFFE are listed in Tables 3–6, and the average for blue and red stars are plotted in Figure 2, for both NGC 6934 and NGC 1261. Internal uncertainties in chemical abundances due to the adopted model atmospheres were estimated by varying the stellar parameters one at a time by the amounts derived in Section 3. In addition to the contribution introduced by internal errors in atmospheric parameters, we estimated the contribution due to the finite signal-to-noise ratio that affects the measurements of EWs and the spectral synthesis. For the species inferred from spectral synthesis we have varied the continuum at the $\pm 1\sigma$ level, and re-derived the chemical abundances from each line. For the elements with a number of available lines $\geqslant 5$ we assume the rms of the average abundance inferred from individual spectral features divided by $\sqrt{N_{\rm lines}}$ as an estimate of the internal errors associated with the errors in the EW measurements. For elements with only a few lines available, we follow the approach by Norris et al. (2010) and Yong et al. (2013): for each element, we replace the rms in Tables 3–5 with the maximum value. Then, we derive $\max({\rm rms})/\sqrt{N_{\rm lines}}$. Since the EWs/continuum placement errors are random, the error associated with those elements with a larger number of lines, e.g., Fe I, is lower. The typical values obtained for each element are listed in Table 7. The total error is obtained by quadratically adding this random error to the uncertainties introduced by atmospheric parameters.

5. Chemical Composition of NGC 6934

The mean metallicity obtained from the UVES sample in NGC 6934 is $[{\rm Fe/H}] = -1.43 \pm 0.05$ dex (rms = 0.12 dex), which is consistent with the two RGB stars observed with MIKE@Magellan (Bernstein et al. 2003) by Marino et al. (2018).[8]

The four UVES stars in the red ChM sequence have $[{\rm Fe/H}] = -1.34 \pm 0.02$ dex (rms = 0.03 dex), while for the three blue-RGB stars we have inferred a mean iron abundance of $[{\rm Fe/H}] = -1.55 \pm 0.03$ dex (rms = 0.04 dex). Quantitatively, we obtain $\Delta[{\rm Fe/H}]_{\rm I} = 0.21 \pm 0.04$ dex, which is more than 5σ level. These results suggest that the red-RGB stars are enriched in the overall metallicity, corroborating with higher statistical significance, the results by Marino et al. (2018).

The presence of a difference in metallicity between the blue and red stars on the ChM is further reinforced by the GIRAFFE

[8] As discussed in Marino et al. (2018), the GRACES@Gemini (Chené et al. 2014) values are systematically higher by ∼0.20 dex. The two stars belonging to the red ChM sequence observed in Marino et al. (2018), namely NGC 6934-a1 and NGC 6934-a2, have been re-observed with UVES and have $[{\rm Fe/H}] = -1.30 \pm 0.01$ dex (#27) and $[{\rm Fe/H}] = -1.35 \pm 0.01$ dex (#47), respectively. The abundances reported in Marino et al. (2018) for these two stars are $[{\rm Fe/H}] = -1.10 \pm 0.02$ dex for NGC 6934-a1 (from GRACES spectra), and $[{\rm Fe/H}] = -1.35 \pm 0.01$ dex for NGC 6934-a2 (from MIKE spectra, for the same star the GRACES value is higher by 0.21 dex). Thus, we conclude that Fe abundances agree between the stars observed with UVES and with MIKE, while there is a systematic offset by 0.20 dex with GRACES spectra.

Table 3
Analyzed Chemical Abundances from O to Sc

Star	[O/Fe]	σ	#	[Na/Fe] LTE	σ	[Na/Fe] Non-LTE	σ	#	[Mg/Fe]	σ	#	[Al/Fe]	σ	#	[Si/Fe]	σ	#	[Ca/Fe]	σ	#	[Sc/Fe]II	σ	#
NGC 6934-37	0.55	0.05	2	0.18	0.04	0.10	0.01	4	0.33	0.03	2	−0.10	0.11	2	0.36	0.10	8	0.32	0.14	20	0.02	0.14	7
NGC 6934-29	0.57	0.17	2	0.53	0.11	0.41	0.08	4	0.33	0.05	2	⋯	⋯	⋯	0.35	0.06	5	0.29	0.12	20	0.07	0.19	6
NGC 6934-27	0.70	0.13	2	−0.23	0.09	−0.30	0.07	4	0.32	0.04	2	0.00	⋯	1	0.36	0.10	5	0.33	0.13	20	0.00	0.14	7
NGC 6934-14	0.44	0.03	2	0.32	0.02	0.24	0.01	4	0.43	0.12	2	0.29	0.01	2	0.42	0.09	8	0.25	0.10	20	−0.03	0.11	7
NGC 6934-1	0.51	0.01	2	0.26	0.03	0.18	0.02	4	0.43	0.04	2	0.20	0.02	2	0.39	0.11	7	0.28	0.07	20	0.02	0.11	7
NGC 6934-5	0.62	0.06	2	−0.07	0.05	−0.13	0.03	4	0.45	0.07	2	−0.07	0.02	2	0.44	0.11	7	0.23	0.09	20	−0.04	0.10	7
NGC 6934-47	0.61	0.08	2	−0.14	0.04	−0.20	0.03	4	0.40	0.08	2	−0.17	⋯	1	0.34	0.08	7	0.33	0.11	20	0.04	0.12	7
Avg.	0.57			0.12		0.04			0.38			0.03			0.38			0.29			0.01		
±	0.03			0.11		0.11			0.02			0.08			0.02			0.02			0.02		
σ	0.08			0.28		0.26			0.06			0.18			0.04			0.04			0.04		
NGC 1261-14	0.05	⋯	1	0.62	0.10	0.51	0.03	4	0.36	0.00	2	0.33	0.06	2	0.35	0.08	8	0.34	0.12	20	0.08	0.13	6
NGC 1261-15	0.39	0.04	2	0.49	0.10	0.38	0.04	4	0.42	0.06	2	0.21	0.03	2	0.43	0.11	6	0.28	0.10	19	0.08	0.11	6
NGC 1261-17	0.20	⋯	1	0.69	0.10	0.56	0.02	4	0.43	0.08	2	0.25	0.05	2	0.42	0.14	6	0.34	0.11	20	0.11	0.11	6
NGC 1261-36	0.48	0.07	2	0.37	0.11	0.27	0.05	4	0.41	0.02	2	0.13	0.06	2	0.38	0.08	5	0.29	0.10	20	0.06	0.12	6
NGC 1261-49	0.56	0.02	2	−0.05	0.07	−0.12	0.04	4	0.45	0.03	2	−0.09	0.04	2	0.44	0.11	6	0.26	0.10	19	0.04	0.11	5
NGC 1261-52	0.12	⋯	1	0.73	0.11	0.59	0.03	4	0.39	0.01	2	0.16	0.03	2	0.39	0.09	8	0.36	0.12	20	0.03	0.15	5
NGC 1261-6	0.55	0.02	2	−0.06	0.07	−0.13	0.06	4	0.40	0.09	2	−0.15	0.03	2	0.41	0.12	6	0.26	0.10	20	0.07	0.10	5
Avg.	0.34			0.40		0.29			0.41			0.12			0.40			0.30			0.07		
±	0.09			0.14		0.13			0.01			0.07			0.01			0.02			0.01		
σ	0.21			0.33		0.31			0.03			0.18			0.03			0.04			0.03		

Table 4
Analyzed Chemical Abundances from Ti to Ni

Star	[Ti/Fe]I	σ	#	[Ti/Fe]II	σ	#	[V/Fe]	σ	#	[Cr/Fe]I	σ	#	[Cr/Fe]II	σ	#	[Mn/Fe]	σ	#	[Co/Fe]	σ	#	[Ni/Fe]	σ	#
NGC 6934-37	0.21	0.12	23	0.21	0.04	5	0.08	0.09	14	−0.17	0.11	5	0.14	0.04	2	−0.52	0.11	5	−0.07	0.08	2	−0.02	0.12	25
NGC 6934-29	0.20	0.14	19	0.21	0.16	5	−0.02	0.11	14	−0.15	0.05	4	0.19	⋯	1	−0.52	0.08	5	−0.07	⋯	1	−0.02	0.10	21
NGC 6934-27	0.18	0.11	23	0.26	0.13	5	−0.03	0.09	14	−0.13	0.08	4	0.22	0.07	2	−0.51	0.07	5	−0.09	0.07	2	−0.04	0.12	23
NGC 6934-14	0.17	0.09	22	0.26	0.10	5	−0.04	0.11	15	−0.14	0.11	5	0.01	0.07	2	−0.55	0.12	5	−0.15	0.04	2	−0.03	0.09	25
NGC 6934-1	0.22	0.10	23	0.30	0.06	5	0.05	0.08	14	−0.15	0.04	5	0.17	0.06	2	−0.47	0.08	5	−0.07	0.03	2	−0.03	0.11	24
NGC 6934-5	0.31	0.14	22	0.22	0.04	4	0.09	0.12	14	−0.15	0.09	4	0.16	0.02	2	−0.47	0.12	5	−0.04	0.08	2	0.01	0.11	25
NGC 6934-47	0.20	0.10	23	0.18	0.07	5	0.01	0.08	14	−0.08	0.10	4	0.25	0.07	2	−0.47	0.07	5	−0.05	0.01	2	−0.03	0.10	24
avg.	0.21			0.23			0.02			−0.14			0.16			−0.50			−0.08			−0.02		
±	0.02			0.02			0.02			0.01			0.03			0.01			0.01			0.01		
σ	0.05			0.04			0.05			0.03			0.08			0.03			0.04			0.02		
NGC 1261-14	0.25	0.12	24	0.24	0.04	5	0.13	0.11	14	−0.14	0.08	4	0.08	0.08	2	−0.41	0.07	5	−0.09	0.06	2	−0.03	0.11	25
NGC 1261-15	0.32	0.11	21	0.27	0.08	4	0.28	0.23	13	−0.10	0.05	4	0.16	0.13	2	−0.37	0.09	5	−0.05	0.14	2	−0.03	0.11	24
NGC 1261-17	0.25	0.11	22	0.20	0.07	5	0.12	0.10	13	−0.11	0.06	4	0.07	0.05	2	−0.44	0.05	5	−0.10	0.05	2	−0.04	0.12	22
NGC 1261-36	0.28	0.12	24	0.24	0.06	5	0.19	0.13	13	−0.12	0.04	4	0.13	0.02	2	−0.38	0.07	5	−0.01	0.10	2	0.00	0.10	25
NGC 1261-49	0.32	0.14	22	0.27	0.09	5	0.23	0.22	13	−0.13	0.09	4	0.17	0.08	2	−0.42	0.09	5	−0.03	0.08	2	−0.02	0.10	24
NGC 1261-52	0.26	0.12	23	0.25	0.07	5	0.09	0.10	14	−0.09	0.05	3	0.15	0.06	2	−0.42	0.04	5	−0.13	0.05	2	0.00	0.11	22
NGC 1261-6	0.33	0.14	23	0.24	0.05	5	0.21	0.23	14	−0.12	0.09	4	0.15	0.14	2	−0.40	0.08	5	−0.08	0.15	2	−0.03	0.11	25
Avg.	0.29			0.24			0.18			−0.12			0.13			−0.41			−0.07			−0.02		
±	0.01			0.01			0.03			0.01			0.02			0.01			0.02			0.01		
σ	0.04			0.02			0.07			0.02			0.04			0.02			0.04			0.02		

Table 5
Analyzed Chemical Abundances from Cu to Eu

Star	[Cu/Fe]	σ	#	[Zn/Fe]	[Y/Fe]	σ	#	[Zr/Fe]	[Ba/Fe]	σ	#	[La/Fe]	σ	#	[Ce/Fe]	σ	#	[Pr/Fe]	[Nd/Fe]	σ	#	[Eu/Fe]	σ	#
NGC 6934-37	−0.64	0.08	2	⋯	−0.19	0.19	3	0.36	0.08	0.05	3	0.21	0.08	6	0.10	0.01	2	0.28	0.35	0.02	2	0.62	0.06	2
NGC 6934-29	−0.57	0.25	2	⋯	−0.12	0.25	3	0.25	0.22	0.05	3	0.29	0.09	5	⋯	⋯	⋯	0.39	0.20	0.01	2	0.70	⋯	1
NGC 6934-27	−0.56	0.16	2	⋯	−0.20	0.25	3	0.23	0.19	0.01	3	0.24	0.06	7	0.13	0.26	2	0.40	0.37	0.03	2	0.61	0.01	2
NGC 6934-14	−0.65	0.27	2	⋯	−0.11	0.07	3	0.20	0.19	0.04	3	0.19	0.09	7	0.09	0.17	2	0.23	0.22	0.08	2	0.45	0.08	2
NGC 6934-1	−0.46	0.12	2	0.03	−0.11	0.14	3	0.40	0.25	0.04	3	0.28	0.08	7	0.13	0.05	2	0.34	0.33	0.00	2	0.61	0.02	2
NGC 6934-5	−0.51	0.08	2	0.14	−0.09	0.22	3	0.40	0.18	0.02	3	0.26	0.06	7	0.12	0.02	2	0.35	0.45	⋯	1	0.62	0.05	2
NGC 6934-47	−0.52	0.33	2	⋯	−0.13	0.16	3	0.31	0.17	0.03	3	0.25	0.08	7	0.18	⋯	1	0.29	0.39	0.01	2	0.59	0.03	2
Avg.	−0.56			0.09	−0.14			0.31	0.18			0.25			0.13			0.33	0.33			0.60		
±	0.03			0.11	0.02			0.03	0.02			0.01			0.01			0.03	0.04			0.03		
σ	0.07			⋯	0.04			0.08	0.05			0.04			0.03			0.06	0.09			0.07		
NGC 1261-14	−0.53	0.39	2	−0.01	−0.09	0.14	3	0.23	0.17	0.03	3	0.33	0.13	7	0.15	0.05	2	0.35	0.43	0.09	2	0.63	0.00	2
NGC 1261-15	−0.48	0.22	2	0.14	−0.06	0.26	3	0.26	−0.07	0.06	3	0.33	0.10	7	0.12	0.02	2	0.42	0.55	⋯	1	0.66	0.04	2
NGC 1261-17	−0.44	0.26	2	0.05	−0.10	0.17	3	0.22	0.15	0.03	3	0.27	0.13	7	0.17	0.04	2	0.36	0.43	0.02	2	0.63	0.02	2
NGC 1261-36	−0.47	0.23	2	0.00	−0.12	0.18	3	0.27	0.09	0.07	3	0.33	0.12	7	0.16	0.05	2	0.43	0.54	0.02	2	0.70	0.03	2
NGC 1261-49	−0.52	0.16	2	0.05	−0.03	0.22	3	0.30	−0.06	0.08	3	0.33	0.09	7	0.13	0.01	2	0.40	0.54	⋯	1	0.69	0.03	2
NGC 1261-52	−0.40	0.21	2	⋯	−0.04	0.17	3	0.24	0.22	0.07	3	0.34	0.11	7	0.17	0.01	2	0.34	0.37	0.00	2	0.66	0.02	2
NGC 1261-6	−0.45	0.22	2	−0.02	−0.05	0.26	3	0.25	−0.08	0.08	3	0.29	0.10	7	0.12	0.00	2	0.33	0.48	0.05	2	0.64	0.02	2
Avg.	−0.47			0.04	−0.07			0.25	0.06			0.32			0.15			0.38	0.48			0.66		
±	0.02			0.03	0.01			0.01	0.05			0.01			0.01			0.02	0.03			0.01		
σ	0.05			0.06	0.03			0.03	0.13			0.03			0.02			0.04	0.07			0.03		

Table 6
Chemical Abundances Obtained with GIRAFFE

GC	Star	[O/Fe]	σ	#	$[Na/Fe]_{LTE}$	σ	$[Na/Fe]_{NLTE}$	σ	#
NGC 6934	22	...	...	...	0.46	0.03	0.39	0.02	2
NGC 6934	23	0.56	0.05	2	...	...	...	...	...
NGC 6934	34	0.35	...	1	0.34	0.17	0.27	0.17	2
NGC 6934	35	0.15	...	1	0.43	0.02	0.37	0.02	2
NGC 6934	42	0.55	0.10	2	0.10	0.01	0.05	0.01	2
NGC 6934	50	0.28	...	1	0.39	0.09	0.31	0.09	2
NGC 1261	7	0.47	0.25	2	−0.01	0.01	−0.08	0.01	2
NGC 1261	22	0.64	0.10	2	0.06	0.03	0.00	0.03	2
NGC 1261	24	0.26	0.05	2	0.14	0.07	0.10	0.07	2
NGC 1261	35	0.62	0.12	2	−0.05	0.03	−0.12	0.03	2
NGC 1261	40	0.31	0.11	2	0.26	0.04	0.21	0.04	2
NGC 1261	54	...	...	0	0.55	0.11	0.47	0.11	2
NGC 1261	61	0.58	0.08	2	−0.26	0.12	−0.31	0.12	2

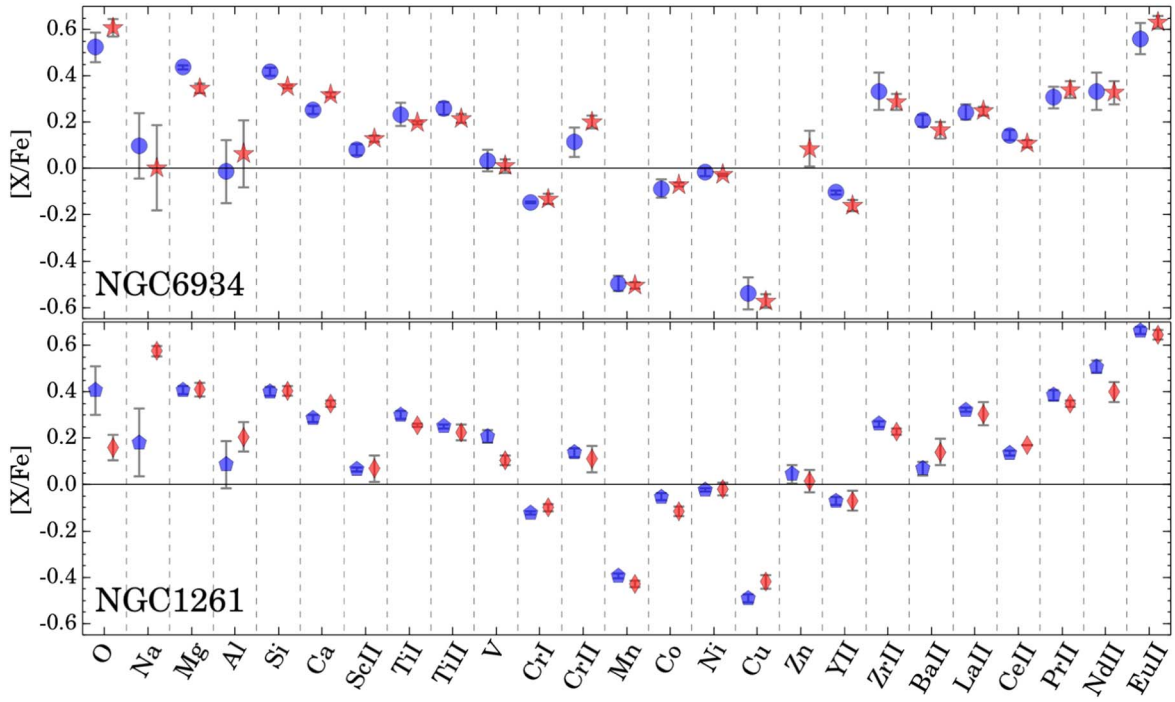

Figure 2. Summary of the abundance ratios results obtained from the UVES spectra. For each species, we plot the [X/Fe] relative abundances. Red symbols are used for stars located on the red sequence of the ChM and filled blue symbols denote stars on the blue sequence.

targets, all belonging to the blue (*normal*) population. For these stars we get an average iron abundance of $[Fe/H] = -1.62 \pm 0.02$ dex (rms = 0.05 dex), within 2σ from the value obtained from UVES, and with a comparable rms, which is much smaller than that obtained for the whole UVES sample.

The Na–O abundances plotted in Figure 3 show the typical anticorrelation pattern observed in GCs. The stars both in the red and in the blue sequence have a range in Na. This is the first detection of internal variations in light elements in the *anomalous* population of NGC 6934 as the targets of Marino et al. (2018) were selected to be located in the lower part of the ChM with relatively low $\Delta_{CF275W,F336W,F438W}$ values, where we did not expect such variations. The middle panel of Figure 3 displays a clear correlation that is present between the $\Delta_{CF275W,F336W,F438W}$ axis of the ChM and the Na abundances, as found for all the analyzed Milky Way GCs (Marino et al. 2019a). Beside the higher $\Delta_{F275W,F814W}$ values on the map, the red stars have on average higher O abundances, as shown in the right panel of Figure 3.

Figure 2 displays a summary of the other chemical abundance ratios as the mean of the three blue-RGB (or *normal*) and the four red-RGB (or *anomalous*) stars (top panel). Chemical abundances relative to Fe for the two groups are consistent within the observational errors for all the analyzed species. Large spreads are observed in Na and Al for both the *normal* and the four *anomalous* stars. Interestingly, there is no evidence for variations in the *neutron*-capture elements between the blue and red stars. This result is consistent with what was found in Marino et al. (2018), who analyzed two red stars in the low $\Delta_{CF275W,F336W,F438W}$ region of the map, not finding any evidence of internal enrichment in the *s*-process elements. The authors, however, could not exclude *s*-process element enrichment at a higher $\Delta_{CF275W,F336W,F438W}$ level of the ChM, a region which they did not explore. The near identity of the abundances of most

Table 7
Sensitivity of the Derived Abundances from UVES Spectra to the Uncertainties in Atmospheric Parameters ($T_{\rm eff}$/log g/$\xi_{\rm t}$/[A/H] = ±50 K/±0.15 dex/±0.20 km s^{-1}/±0.10 dex), and Uncertainties due to the Errors in the EW Measurements or in the χ-square Fitting Procedure

	$\Delta T_{\rm eff}$ ±100 K	$\Delta T_{\rm eff}$ ±50 K	Δ log g ±0.15	$\Delta\xi_{\rm t}$ ±0.20 km s^{-1}	Δ[A/H] ±0.10 dex	$\sigma_{\rm EWs/fit}$	$\sigma_{\rm total}$
[O/Fe]	±0.02	±0.01	±0.07	±0.00	±0.03	±0.05	±0.09
[Na/Fe]	∓0.02	∓0.01	∓0.02	±0.04	±0.03	±0.04	±0.07
[Mg/Fe]	∓0.02	∓0.01	∓0.03	∓0.01	∓0.00	±0.08	±0.09
[Al/Fe]	±0.07	±0.05	∓0.01	±0.00	±0.01	±0.08	±0.12
[Si/Fe]	∓0.09	∓0.06	±0.01	±0.06	±0.01	±0.04	±0.09
[Ca/Fe]	±0.02	±0.01	∓0.02	∓0.02	∓0.01	∓0.02	±0.04
[Sc/Fe] II	±0.07	±0.04	∓0.01	±0.01	∓0.01	±0.07	±0.08
[Ti/Fe] I	±0.09	±0.05	∓0.02	±0.01	∓0.01	±0.03	±0.06
[Ti/Fe] II	±0.05	±0.03	∓0.02	∓0.02	∓0.02	±0.06	±0.07
[V/Fe]	±0.10	±0.05	∓0.01	±0.03	±0.03	±0.06	±0.08
[Cr/Fe] I	±0.07	±0.03	∓0.02	∓0.01	∓0.02	∓0.06	±0.07
[Cr/Fe] II	±0.01	±0.01	∓0.01	±0.02	∓0.02	±0.10	±0.10
[Mn/Fe]	±0.15	±0.07	∓0.00	∓0.01	∓0.02	±0.05	±0.09
[Fe/H] I	±0.10	±0.05	±0.01	∓0.07	±0.00	±0.01	±0.09
[Fe/H] II	∓0.09	∓0.05	±0.07	∓0.05	±0.04	±0.03	±0.11
[Co/Fe]	±0.00	∓0.00	∓0.00	±0.05	±0.01	±0.10	±0.11
[Ni/Fe]	∓0.03	∓0.02	±0.01	±0.04	±0.01	±0.03	±0.05
[Cu/Fe]	±0.11	±0.05	∓0.02	∓0.04	∓0.03	±0.11	±0.13
[Zn/Fe]	∓0.12	∓0.06	±0.00	±0.05	±0.01	±0.15	±0.17
[Y/Fe] II	±0.08	±0.05	∓0.01	∓0.01	∓0.01	±0.15	±0.16
[Zr/Fe] II	∓0.15	∓0.08	±0.12	∓0.02	±0.05	±0.10	±0.18
[Ba/Fe] II	±0.03	±0.02	±0.07	∓0.14	±0.03	±0.10	±0.19
[La/Fe] II	±0.02	±0.01	±0.05	∓0.01	±0.03	±0.02	±0.06
[Ce/Fe] II	±0.01	±0.00	±0.06	∓0.01	±0.04	±0.10	±0.12
[Pr/Fe] II	±0.02	±0.01	±0.06	±0.00	±0.05	±0.10	±0.13
[Nd/Fe] II	±0.12	±0.06	∓0.01	∓0.02	∓0.01	±0.06	±0.09
[Eu/Fe] II	∓0.01	±0.00	±0.06	±0.00	±0.04	±0.09	±0.12

Note. For reference, we also list the variations due to a change in $T_{\rm eff}$ by ±100 K. We reported the total internal uncertainty ($\sigma_{\rm total}$) obtained by the quadratic sum of all the contributers to the error.

elements in the blue and red populations excludes the possibility that the red sequence was accreted from outside, instead assuming that it was formed from material enriched in metallicity, possibly by supernovae from the blue-sequence population.

In the left panel of Figure 4 we plot the [La/Fe] of NGC 6934, assuming La as a representative of the *s*-elements, versus [Fe/H]. Clearly, while all four red stars have higher Fe, they have similar La, independently of their location along the $\Delta_{CF275W,F336W,F438W}$ axis of the ChM. This result confirms that NGC 6934 shows no evidence of additional internal variations in *s*-process elements.

6. Chemical Composition of NGC 1261

The average Fe abundance for the giants analyzed with UVES in NGC 1261 is [Fe/H] = −1.28 ± 0.02 (rms = 0.05). By dividing the sample into *normal* and *anomalous* stars, we get mean Fe abundances of [Fe/H] = −1.30 ± 0.01 dex (rms = 0.03, five stars) and [Fe/H] = −1.22 ± 0.01 dex (two stars), respectively. Although the difference between the two groups goes in the direction observed for nearly all Type II GCs, i.e., the *anomalous* stars are Fe-richer, the small sample of stars (only two in the red sequence) and the small difference (<0.10 dex) prevent us from drawing definitive conclusions about a possible enrichment in Fe among the red-sequence stars of this cluster by using spectroscopy alone. Nevertheless, the slightly higher Fe of two stars and their concurrent position on the red side of the ChM suggest a small Fe enrichment in these stars.

For the seven stars analyzed with GIRAFFE we obtain an average Fe I abundance of [Fe/H] = −1.35 ± 0.02 (rms = 0.04). These stars all belong to the blue sequence on the ChM. Hence, a comparison with the UVES chemical abundances is more appropriate by considering only the blue-sequence stars in that sample. The average Fe abundances of the two samples agree at a 2σ level.

Similar to what was displayed for NGC 6934, the lower panel of Figure 2 shows the mean abundances obtained for the blue-sequence and red-sequence stars of NGC 1261 from UVES spectra. We note that the overall chemical pattern between the two clusters is similar.

Large spreads are observed in the light elements O, Na, and Al, while the Mg abundance range is narrow both among the *normal* and the *anomalous* stars. In the lower panels of Figure 3 we show the Na–O anticorrelation obtained from both the UVES and GIRAFFE data, as well as the Na and O abundances as a function of $\Delta_{CF275W,F336W,F438W}$ and $\Delta_{F275W,F814W}$, respectively. The two red stars also have the highest Na abundances, consistent with their higher $\Delta_{CF275W,F336W,F438W}$ values on the ChM. They are among the most O-depleted stars in the sample, not following the mild O–$\Delta_{F275W,F814W}$ correlation defined by the blue stars.

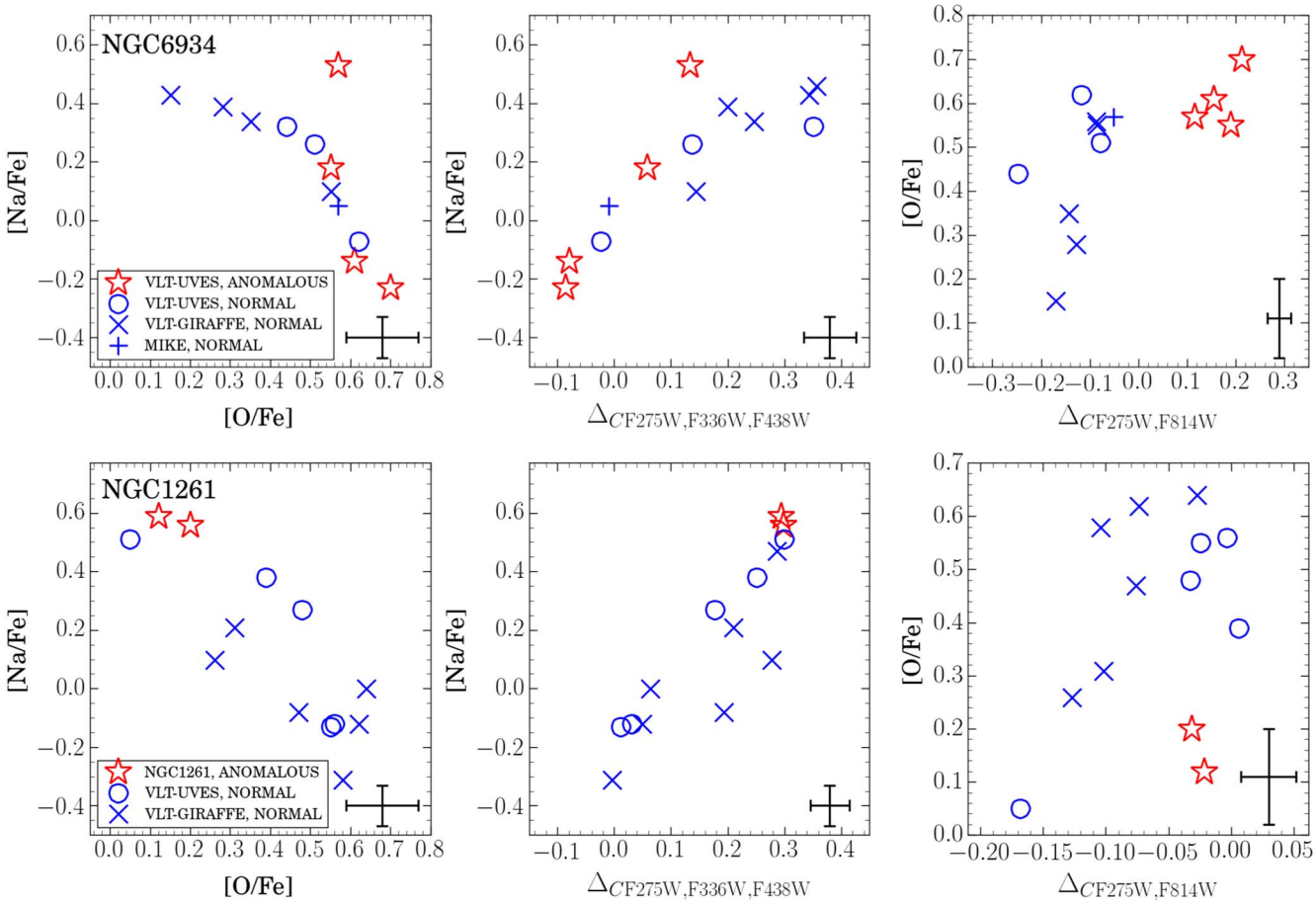

Figure 3. Na–O anticorrelation obtained for NGC 6934 (upper left panel) and NGC 1261 (bottom left panel). The middle and right panels represent the [Na/Fe] and [O/Fe] abundance as a function of the $\Delta_{CF275W,F336W,F438W}$ and $\Delta_{F275W,F814W}$ axis of the ChM, respectively, for NGC 6934 (upper panels) and NGC 1261 (bottom panels). Blue and red symbols represent the targets on the blue and red sequence of the CMD and the ChM in both GCs.

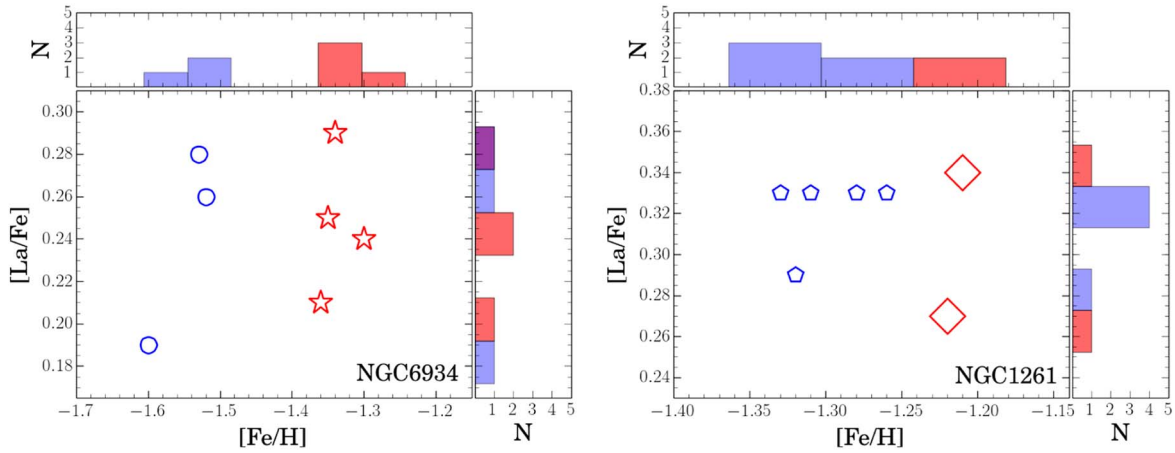

Figure 4. Lanthanum abundance as a function of [Fe/H] for NGC 6934 (left) and NGC 1261 (right). Blue- and red-sequence stars are represented with blue and red symbols, respectively. The histograms represent the distribution of [Fe/H] and [La/Fe] of stars in the corresponding ChM sequence.

Again, we do not find any evidence of internal variation in the *n*-capture elements, as also suggested by the [La/Fe] versus [Fe/H] plot displayed in Figure 4.

The homogeneous content of *s*-elements may provide further constraints on iron variations in NGC 1261. Indeed, *s*-element enhancement is likely due to intermediate-mass AGB stars and is associated with enhancement in the overall C+N+O content (e.g., Ventura et al. 2009). The fact that blue-RGB and red-RGB stars share the same [La/Fe] content may suggest that all NGC 1261 stars share the same overall CNO abundance. Assuming constant C+N+O, iron variation is possibly the only parameter responsible for the SGB split. As shown in Figure 5, the faint SGB and the red RGB of NGC 1261 are consistent with an isochrone with the same age (12.75 Gyr) and [α/Fe] $= 0.4$ as the blue RGB and the bright SGB, but enhanced in [Fe/H] by 0.1 dex. This result corroborates the finding from

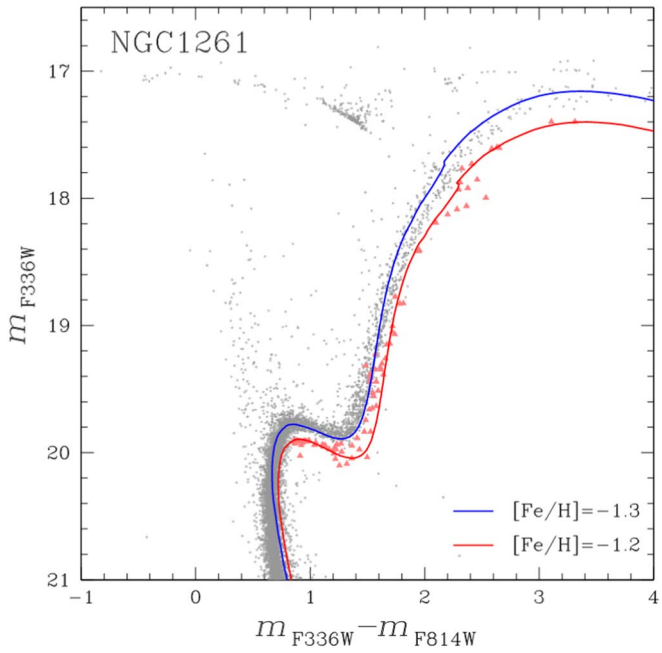

Figure 5. Comparison between the CMD of NGC 1261 and isochrones from Dotter et al. (2008). Faint-SGB and red-RGB stars are represented with red symbols. The red and blue isochrones have the same ages of 12.75 Gyr but different iron abundances of [Fe/H] = −1.2 and [Fe/H] = −1.3, respectively.

spectroscopy that red-RGB stars are more iron-rich than the blue RGB.

7. Discussion and Conclusions

Chemical enrichment of iron has been found to be a feature of Type II GCs, which have stars distributed on the redder side of the ChM enhanced in metallicity. The fact that Type II GCs are among the most massive clusters in the Milky Way is reminiscent of the idea that more massive objects are more efficient in retaining the ejecta from SNe, though not all massive GCs are Type II (Milone et al. 2017).

Figure 6 shows the distributions in present-day masses of Galactic GCs, with Type II GCs indicated by the red filled histogram. One can see that NGC 6934 and NGC 1261 are among the lowest-mass Type II GCs identified so far, but still more massive than $10^5 M_\odot$.

For NGC 6934 we confirm that the stars on the red side of the map have iron abundances higher than the bulk of the stars in the clusters defining the blue sequence on the ChM. The observed enrichment in Fe is Δ[Fe/H] = +0.21 ± 0.04 dex. Some hint of a small Fe enrichment, by Δ[Fe/H] = +0.08 ± 0.01 dex has also been detected in the red RGB of NGC 1261, although having only two stars makes it difficult to draw strong conclusions from spectroscopy alone.

However, we notice that the analyzed stars are homogeneous in *s*-process elements, which would suggest that red- and blue-RGB stars have constant C+N+O content (e.g., Cassisi et al. 2008; Ventura et al. 2009; Yong et al. 2009). If this hypothesis is correct, the only way to reproduce the photometric splits on the SGB and the RGB is to assume that red-RGB/faint-SGB stars are enhanced in [Fe/H] by ∼0.1 dex. This fact would corroborate the spectroscopic evidence of a metallicity variation in NGC 1261.

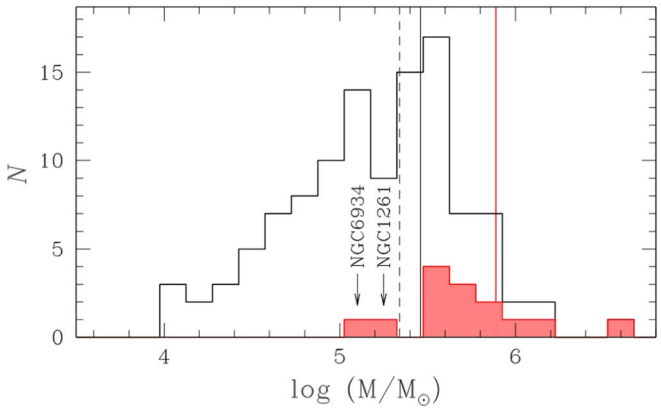

Figure 6. Histogram distributions of present-day masses for Milky Way GCs (black) and for Type II GCs (red filled histogram). Gray dashed and red continuous vertical lines indicate the average masses of these two groups of GCs, whereas the continuous vertical line marks the average mass of all clusters. GC masses are from Baumgardt & Hilker (2018).

Following the approach introduced in Renzini (2008), we calculate for the two analyzed and eight more Type II GCs the excess iron content (Fe_{plus}) of the red-sequence population in these clusters. This is defined as:

$$Fe_{plus} = Z_{Fe}^{R} - Z_{Fe}^{B} M_R \quad (1)$$

where Z_{Fe}^{R} and Z_{Fe}^{B} are the iron abundance masses in the blue sequence and in the red sequence, respectively, and M_R is the mass of the red sequence from Milone et al. (2017). Results are provided in Table 8. As suggested by Renzini (2008), this quantity can be related to the iron produced by the core-collapse supernovae of the blue-sequence population.

Figure 7 displays the additional Fe in the red stars of 10 Type II GCs as a function of their present-day mass with both quantities on a logarithmic scale. As discussed above, the values Fe_{plus} have been calculated as the Fe mass fraction of the red stars on the ChMs multiplied by the stellar mass in the corresponding population.[9] There is a quite clear correlation among the two plotted quantities, with the more massive GCs showing higher Fe_{plus}, which means higher Fe-enriched stellar masses. NGC 6934 and NGC 1261 have the lowest Fe-enriched mass. A possible exception is NGC 362, which is consistent with having constant iron abundance (Marino et al. 2019a).

Translating the Fe_{plus} in each cluster into the fraction of Fe produced by SNe II that has been retained to form Fe-richer stars,[10] we find that only three clusters, namely NGC 6273, NGC 6715 (M54), and NGC 5139 (ω Centauri), have retained more than the 2% of the SNe II material. Not surprisingly, ω Centauri is the GC that has retained the most material from supernovae. NGC 6273 and M54 have retained around 5% of metal-enriched SNe ejecta and NGC 1851 and NGC 6656 (M22) between 1% and 2%. The clusters analyzed here, NGC 6934 and NGC 1261, are among those that retained a lower amount of material.

[9] In the case of more than one "red sequence" on the ChM, we have considered all the stellar populations. Given the difficulty of selecting individual stellar populations in ω Centauri, for this GC we have considered the 36% of stars with [Fe/H] = −1.85, the 50% with [Fe/H] = −1.50, and the 14% with [Fe/H] = −1.00.

[10] This quantity has been derived assuming that a stellar generation makes ∼0.5 $M_\odot$ of iron from core-collapse supernovae every 1000 $M_\odot$ of gas turned into stars (e.g., Renzini & Andreon 2014, and references therein).

Table 8
Average Iron Abundance of Blue-RGB, Red-RGB, and Extreme Stars and the Corresponding Fractions of Stars in each Population ($\%_{\rm blue\ RGB}$, $\%_{\rm red\ RGB}$, $\%_{\rm extreme}$) for each Type II GC from Milone et al. (2017)

ID	[Fe/H] Blue RGB (dex)	$\%_{\rm blueRGB}$ (%)	[Fe/H] Red RGB (dex)	$\%_{\rm redRGB}$ (%)	[Fe/H] Extreme (dex)	$\%_{\rm extreme}$ (%)	Mass [$\times 10^5 M_\odot$]	$\%_{\rm SNe}$ %	$\rm Fe_{plus}$ ($M_\odot$)	References Fe Abundances
NGC 362	−1.18	92.5	−1.17	7.5	⋯	⋯	3.45	0.03	0.05	Marino et al. (2019a)
NGC 1261	−1.30	96.2	−1.22	3.8	⋯	⋯	1.67	0.10	0.08	This work
NGC 1851	−1.19	70	−1.13	30	⋯	⋯	3.02	1.07	1.13	Carretta et al. (2010b)
NGC 5286	−1.77	83.3	−1.63	16.7	⋯	⋯	4.01	0.34	0.57	Marino et al. (2015)
NGC 6273	−1.77	46	−1.51	48	−1.22	6	6.80	5.28	8.26	Johnson et al. (2017)
NGC 6656	−1.82	59.7	−1.67	40.3	⋯	⋯	4.16	1.10	1.37	Marino et al. (2011b)
NGC 6715	−1.73	54	−1.39	46	⋯	⋯	14.1	4.93	18.8	Marino et al. (2019a)
NGC 6934	−1.55	93.3	−1.34	6.7	⋯	⋯	1.17	0.33	0.18	This work
NGC 7089	−1.68	96	−1.51	3.0	−1.03	1	5.82	0.28	0.78	Yong et al. (2014)
NGC 5139	−1.85	36	−1.50	50	−1.00	14	35.5	15.11	96.5	This work

Note. We also provide the present-day GC mass (from Baumgardt & Hilker 2018), the fraction of the iron produced by SNe that has been retained by the cluster ($\%_{\rm SNe}$), and the corresponding amount of iron in $M_\odot$ ($\rm Fe_{plus}$). The last column provides the reference to the paper where iron abundances of the *normal* and *anomalous* stars are derived. In NGC 5286 only abundances from GIRAFFE data are used.

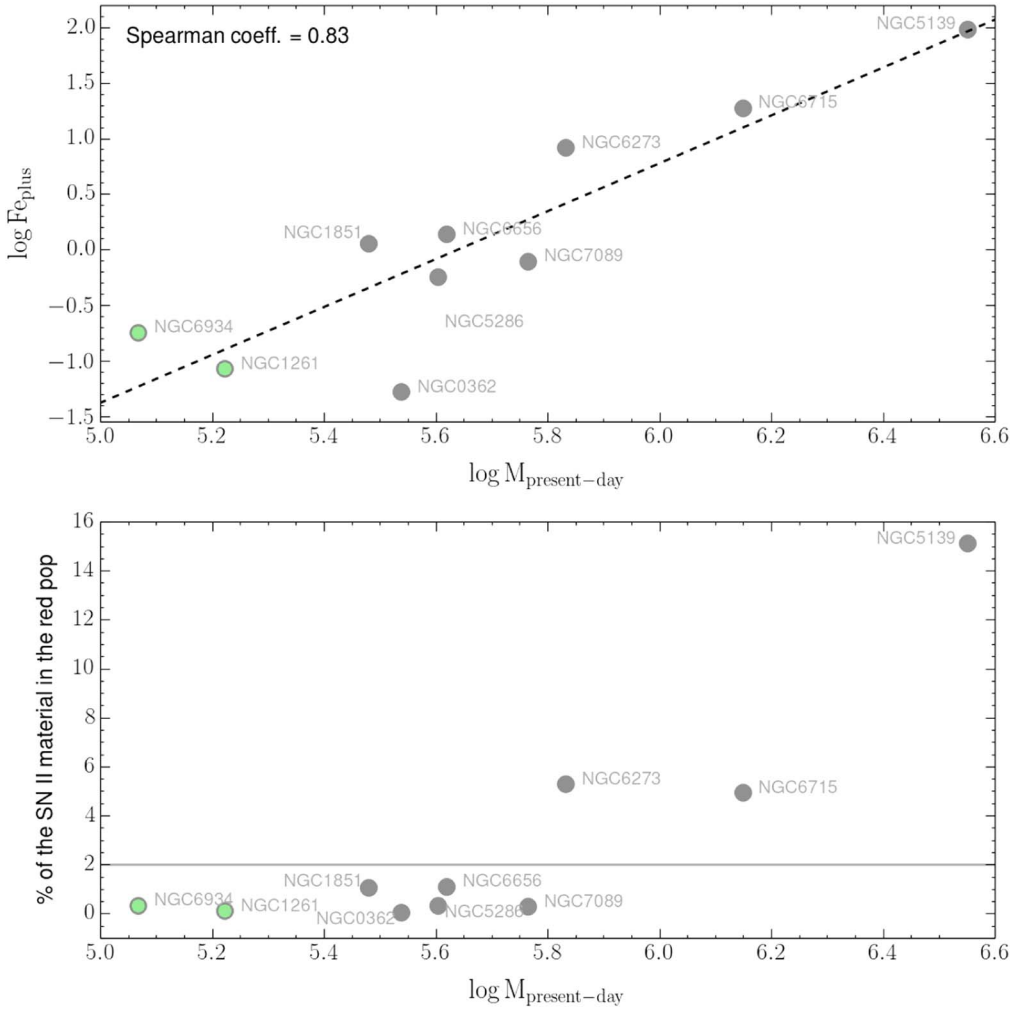

Figure 7. Logarithm of the additional Fe ($\log \rm Fe_{plus}$) in the metal richer stellar populations as a function of the logarithm present-day GC masses. $\rm Fe_{plus}$ has been calculated as the additional mass fraction of Fe multiplied by the fraction of mass in the redder stars (see Table 2 from Milone et al. 2017). Fraction of iron produced by SNe II that has been retained to form the populations enhanced in iron.

We conclude that typically only a few percent of the iron produced by the blue-sequence population was incorporated in the red-sequence population, while all the rest was lost by the system.

Interestingly enough, the two less massive Type II GCs analyzed so far in the context of ChM stellar populations, namely NGC 6934 and NGC 1261, are the only known Type II GCs with no evidence for variations in the *s*-element chemical abundances. This finding may add new insights into the understanding of this class of globular clusters, suggesting that a mass threshold could exist either for the retention of the *s*-process enriched material and/or for the capability of sustaining more prolonged star formation histories with contributions from lower-mass AGB stars.

Furthermore, although La variations are common features of massive Type II GCs, we note that the [La/Fe] difference between red-RGB and blue-RGB stars seems unrelated to the [Fe/H] difference. [La/Fe] varies by ∼0.2 dex (in M2 Yong et al. 2014) up to ∼1.5 dex (in ω Centauri, Marino et al. 2012b). Lanthanum variations of ∼0.3 dex are observed in both NGC 1851, which exhibits tiny Fe differences between red- and blue-RGB stars (∼0.05 dex) and NGC 6656 where we observe a small iron spread relative to M54 of ∼0.15 dex (Yong & Grundahl 2008; Da Costa et al. 2009; Marino et al. 2009, 2011b; Carretta et al. 2010b). Similarly, NGC 5286 shows a large [La/Fe] difference of ∼0.65 dex, and iron variation of ∼0.2 dex (Marino et al. 2015), whereas the large iron variation of NGC 6273 (∼0.5 dex, Johnson et al. 2017) corresponds to a [La/Fe] difference of ∼0.4 dex. However, red-RGB and blue-RGB stars of the Type II GC NGC 362 have the same iron abundance, but different content of s-process elements (Marino et al. 2019a).

We conclude by emphasizing that the total stellar mass of the cluster is indeed a fundamental parameter for shaping the pattern of multiple stellar populations in GCs (see also Milone et al. 2017, 2020; Dondoglio et al. 2021; Lagioia et al. 2021a). This parameter is also relevant within the GCs associated with the newly discovered class of *anomalous* Type II GCs.

1. Type II GCs lie along the more massive side of the Milky Way GC mass distribution.
2. Among these clusters, the more massive the GC is, the higher is the amount of iron that has been incorporated in the red *anomalous* stellar population on the ChM.
3. Only some GCs with present-day total masses $M \gtrsim 10^{5.8} M_{\odot}$ have retained a fraction of SNII material higher than 2%.
4. At odds with the majority of *anomalous*/Type II GCs, the two less massive Type II GCs analyzed so far show no evidence of *s*-process-based enrichment.

We warmly thank the anonymous referee for useful discussions that have improved the quality of the manuscript. This work has received funding from the European Research Council (ERC) under the European Union's Horizon 2020 research innovation program (Grant Agreement ERC-StG 2016, No 716082 "GALFOR," PI: A. P. Milone, http://progetti.dfa.unipd.it/GALFOR). A.P.M. acknowledges support from MIUR through the FARE project R164RM93XW SEMPLICE (PI: A. P. Milone). A.P.M. has been supported by MIUR under PRIN program 2017Z2HSMF (PI: L. R. Bedin).

Appendix
Lanthanum Abundances along the Chromosome Map of M54

As discussed throughout the paper, variations in *s*-process elements have been observed in various Type II GCs and are often associated with variations in the overall CNO content (e.g., Yong & Grundahl 2008; Marino et al. 2009; Yong et al. 2009). In the context of Type II GCs M54 might represent the link between the class of globular cluster and dwarf galaxies, as this GC resides in the nucleus of the Sagittarius dwarf galaxy (Bellazzini et al. 2008). Although M54 has been widely studied in the literature, still the abundance of *s*-elements in its stellar populations has been never investigated.

In the spirit of investigating the nature of Type II GCs, and possibly the relation to their formation environment, we add in this appendix a brief discussion on M54, by exploring the lanthanum abundances of its stellar populations. We use the Fe abundances and atmospheric parameters from Carretta et al. (2010a) to derive first abundances of La by exploiting the GIRAFFE spectra analyzed by the same authors.

Iron abundances, together with light elements, of M54 along the ChM have already been investigated in Marino et al. (2019a), who identified eight stars on the blue RGB and 10 stars on the red one. They found mean [Fe/H] = −1.73 ± 0.06 (rms = 0.16), and [Fe/H] = −1.39 ± 0.03 (rms = 0.11). Figure 8 shows the ChM of

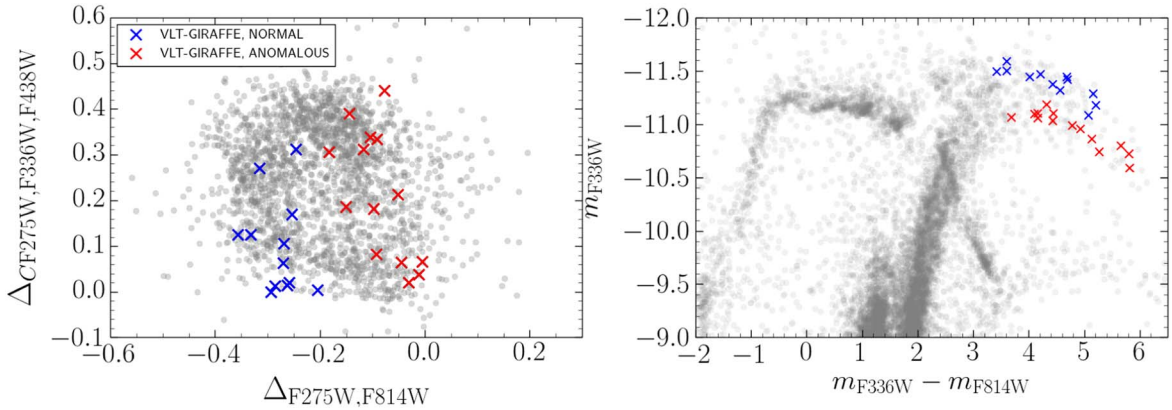

Figure 8. Chromosome map (left panel) and m_{F336W} vs. $m_{F336W} - m_{F814W}$ CMD (right panel) for M54. The stars colored in red have been selected as the stars defining the redder RGB stars on the CMD. Blue and red crosses are the GIRAFFE targets of Carretta et al. (2010a) that we have associated with the red- and blue-RGB/ChM sequence, respectively.

M54 and the m_{F336W} versus $m_{F336W} - m_{F814W}$ CMD for the stars observed with GIRAFFE. Here we identify 12 stars on the blue RGB and 14 on the red one. The presence of more stars with available ChM data than in Marino et al. (2019a) is basically due to our more generous photometric constraints which include a larger range in magnitudes. The zoom-in of a typical spectrum around the La line at 6262 Å has been plotted in Figure 9, where we also show the synthetic spectra that provide the best fit with the observations and the synthetic spectra that differ in [La/Fe] by ±0.2 dex from the best-fit ones.

To derive the internal error associated with the La measurements of M54, we used the uncertainties in the atmospheric parameters of Carretta et al. (2010a), i.e., $\Delta T_{\rm eff}/\Delta \log g/\Delta[{\rm A/H}]/\Delta\xi_{\rm t} = \pm 50$ K/±0.2 dex/±0.1 dex/±0.1 km s^{-1}.

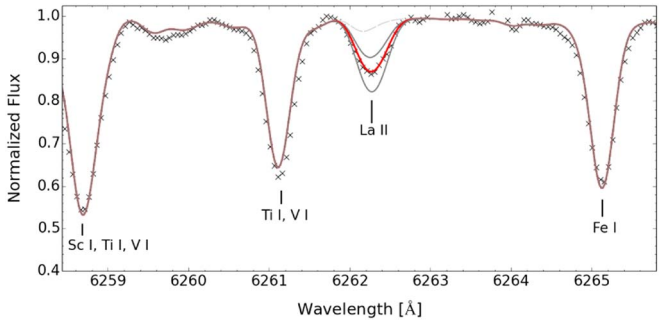

Figure 9. Observed and synthetic spectra around the La line at 6262 Å for star #38000997 in M54 (GIRAFFE data from Carretta et al. 2010a). The cross points represent the observed spectrum, the light-gray dashed line is the spectrum computed with no contribution from La; the red line is the best-fitting synthesis; and the gray lines are the synthetic spectra computed with La abundances altered by ±0.2 dex from the best value. For this synthesis we have assumed [N/Fe] = +0.8 dex.

As expected, [La/Fe] abundances are mostly affected by the uncertainties in the surface gravities, as the values vary by ±0.08 by changing log g by ±0.20 dex. Variations in metallicity by ±0.10 change [La/Fe] by ±0.05, while temperature and microturbulence do not introduce significant uncertainties to the results. The quality of the data affects the results in [La/Fe] by 0.10 dex. The total estimated uncertainty associated with our individual La abundances is 0.14 dex, which is comparable to the rms obtained for the mean La abundance of the blue- and red-RGB stars in M54.

Results are shown in Figure 10, where we represent the [Fe/H] and [La/Fe] as a function of the $\Delta_{F275W,F814W}$ values. As expected, the distribution of stars along $\Delta_{F275W,F814W}$ is sensitive to metallicity. Our mean [Fe/H] for the stars on the ChM of M54 are [Fe/H] = −1.70 ± 0.04 (rms = 0.13) and [Fe/H] = −1.42 ± 0.03 (rms = 0.12), for the blue- and red-RGB, respectively. Lanthanum over iron might be marginally enhanced among Fe-rich stars, being the mean values for blue and red RGBs: [La/Fe] = +0.27 ± 0.04 (rms = 0.15) and [La/Fe] = +0.37 ± 0.04 (rms = 0.15), respectively. However, with the current data set the difference is only at 1.5σ level, preventing any strong conclusion on [La/Fe] variations between red- and blue-RGB stars. Howver, the absolute abundance of La in the two RGBs is significantly different and ranges from [La/H] = −1.43 in the blue RGB to [La/H] = −1.05 in the red RGB.

The possible small [La/Fe] variation observed in M54, which is one of the studied Type II GCs with the biggest iron variation, further suggests that multiple processes may govern the chemical enrichment in Type II GCs (see discussion in Section 7). The s-process enrichment, possibly due to AGB stars, seems to be poorly efficient in M54 despite the significant [Fe/H] spread driven by supernovae. We emphasis that further analysis of the different stellar populations in M54 based on higher-resolution data is mandatory to settle the magnitude of possible variations in neutron-capture elements in this GC.

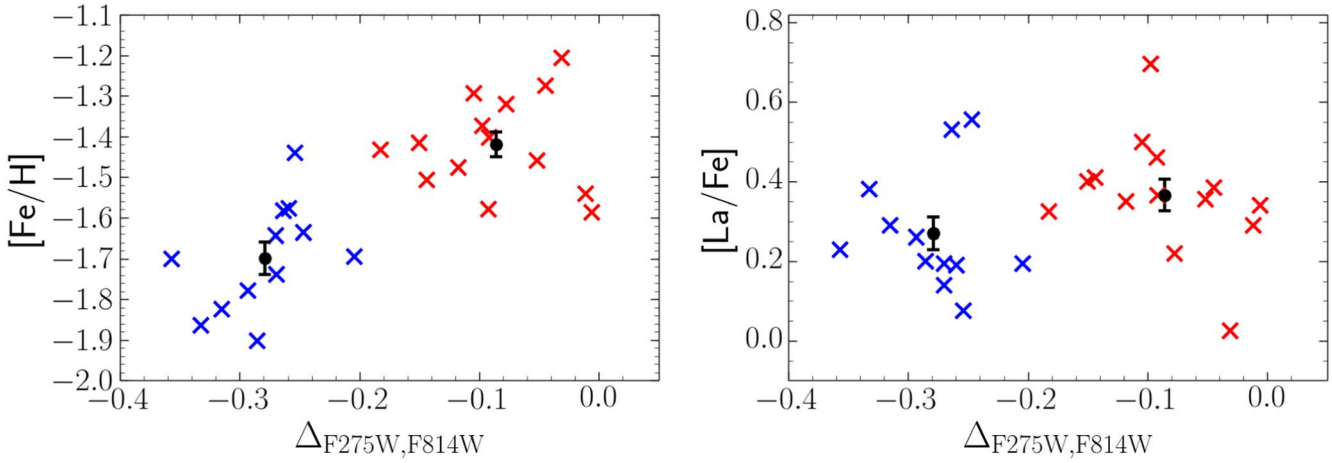

Figure 10. [Fe/H] and [La/Fe] abundances as a function of the $\Delta_{F275W,F814W}$ axis of the ChM for M54. Blue and red crosses represent the stars associated with the red- and blue- RGB/ChM sequence, respectively, as in Figure 8. In each panel, we indicate the mean abundances with the associated error for each group.

ORCID iDs

A. F. Marino https://orcid.org/0000-0002-1276-5487
A. P. Milone https://orcid.org/0000-0001-7506-930X
A. Renzini https://orcid.org/0000-0002-7093-7355
D. Yong https://orcid.org/0000-0002-6502-1406
G. S. Da Costa https://orcid.org/0000-0001-7019-649X
H. Jerjen https://orcid.org/0000-0003-4624-9592
G. Cordoni https://orcid.org/0000-0002-7690-7683
M. Carlos https://orcid.org/0000-0003-1757-6666
E. Dondoglio https://orcid.org/0000-0001-8415-8531
E. P. Lagioia https://orcid.org/0000-0003-1713-0082
S. Jang https://orcid.org/0000-0002-1562-7557
M. Tailo https://orcid.org/0000-0002-1128-098X

References

Alonso, A., Arribas, S., & Martínez-Roger, C. 1999, A&AS, 140, 261
Amarsi, A. M., Asplund, M., Collet, R., & Leenaarts, J. 2016, MNRAS, 455, 3735
Anderson, J., Sarajedini, A., Bedin, L. R., et al. 2008, AJ, 135, 2055
Ballester, P., Modigliani, A., Boitquin, O., et al. 2000, Msngr, 101, 31
Baumgardt, H., & Hilker, M. 2018, MNRAS, 478, 1520
Bekki, K., & Freeman, K. C. 2003, MNRAS, 346, L11
Bellazzini, M., Ibata, R. A., Chapman, S. C., et al. 2008, AJ, 136, 1147
Bergemann, M., Lind, K., Collet, R., Magic, Z., & Asplund, M. 2012, MNRAS, 427, 27
Bernstein, R., Shectman, S. A., Gunnels, S. M., Mochnacki, S., & Athey, A. E. 2003, Proc. SPIE, 4841, 1694
Carretta, E., Bragaglia, A., Gratton, R. G., et al. 2010a, A&A, 520, A95
Carretta, E., Gratton, R. G., Lucatello, S., et al. 2010b, ApJL, 722, L1
Cassisi, S., Salaris, M., Pietrinferni, A., et al. 2008, ApJL, 672, L115
Castelli, F., & Kurucz, R. L. 2004, arXiv:astro-ph/0405087
Chené, A.-N., Padzer, J., Barrick, G., et al. 2014, Proc. SPIE, 9151, 915147
Da Costa, G. S., Held, E. V., Saviane, I., & Gullieuszik, M. 2009, ApJ, 705, 1481
Da Costa, G. S., & Marino, A. F. 2011, PASA, 28, 28
Dekker, H., D'Odorico, S., Kaufer, A., et al. 2000, Proc. SPIE, 4008, 534
Dondoglio, E., Milone, A. P., Lagioia, E. P., et al. 2021, ApJ, 910, 6
Dotter, A., Chaboyer, B., Jevremović, D., et al. 2008, ApJS, 178, 89
Harris, W. E. 1996, AJ, 112, 1487
Harris, W. E. 2010, arXiv:1012.3224
Ibata, R. A., Bellazzini, M., Malhan, K., et al. 2019, NatAs, 3, 667
Johnson, C. I., Caldwell, N., Rich, R. M., & Walker, M. G. 2017, AJ, 154, 155
Johnson, C. I., Caldwell, N., Rich, R. M., et al. 2017, ApJ, 836, 168
Johnson, C. I., & Pilachowski, C. A. 2010, ApJ, 722, 1373
Johnson, C. I., Rich, R. M., Pilachowski, C. A., et al. 2015, AJ, 150, 63
Kausch, W., Noll, S., Smette, A., et al. 2014, in ASP Conf. Ser. 485, Astronomical Data Analysis Software and Systems XXIII, ed. N. Manset & P. Forshay (San Francisco, CA: ASP), 403
Kuzma, P. B., Da Costa, G. S., Mackey, A. D., et al. 2016, MNRAS, 461, 3639
Kuzma, P. B., Da Costa, G. S., & Mackey, A. D. 2018, MNRAS, 473, 2881
Lagioia, E., Milone, A. P., Marino, A. F., et al. 2021a, AJ, 158, 202
Lagioia, E., Milone, A. P., Marino, A. F., et al. 2021b, ApJ, 910, 6
Lind, K., Bergemann, M., & Asplund, M. 2012, MNRAS, 427, 50
Majewski, S. R., Nidever, D. L., Smith, V. V., et al. 2012, ApJL, 747, L37
Marino, A. F., Milone, A. P., Karakas, A. I., et al. 2015, MNRAS, 450, 815
Marino, A. F., Milone, A. P., Piotto, G., et al. 2009, A&A, 505, 1099
Marino, A. F., Milone, A. P., Piotto, G., et al. 2011a, ApJ, 731, 64
Marino, A. F., Milone, A. P., Piotto, G., et al. 2012a, ApJ, 746, 14
Marino, A. F., Milone, A. P., Renzini, A., et al. 2019a, MNRAS, 487, 3815
Marino, A. F., Milone, A. P., Sills, A., et al. 2019b, ApJ, 887, 91
Marino, A. F., Milone, A. P., Sneden, C., et al. 2012b, A&A, 541, A15
Marino, A. F., Milone, A. P., Yong, D., et al. 2014, MNRAS, 442, 3044
Marino, A. F., Sneden, C., Kraft, R. P., et al. 2011b, A&A, 532, A8
Marino, A. F., Villanova, S., Piotto, G., et al. 2008, A&A, 490, 625
Marino, A. F., Yong, D., Milone, A. P., et al. 2018, ApJ, 859, 81
Massari, D., Koppelman, H. H., & Helmi, A. 2019, A&A, 630, 4
Milone, A. P., Bedin, L. R., Piotto, G., et al. 2008, ApJ, 673, 241
Milone, A. P., Marino, A. F., Da Costa, G. S., et al. 2020, MNRAS, 491, 515
Milone, A. P., Marino, A. F., Piotto, G., et al. 2015, MNRAS, 447, 927
Milone, A. P., Piotto, G., Renzini, A., et al. 2017, MNRAS, 464, 3636
Norris, J. E., & Da Costa, G. S. 1995, ApJ, 447, 680
Norris, J. E., Yong, D., Gilmore, G., et al. 2010, ApJ, 711, 350
Olszewski, E. W., Saha, A., Knezek, P., et al. 2009, AJ, 138, 1570
Pasquini, L., Avila, G., Allaert, E., et al. 2000, Proc. SPIE, 4008, 129
Piotto, G., Milone, A. P., Bedin, L. R., et al. 2015, AJ, 149, 91
Renzini, A. 2008, MNRAS, 391, 354
Renzini, A., & Andreon, S. 2014, MNRAS, 444, 358
Smette, A., Sana, H., Noll, S., et al. 2015, A&A, 576, 77
Sneden, C. 1973, ApJ, 184, 839
Ventura, P., Caloi, V., D'Antona, F., et al. 2009, MNRAS, 399, 934
Yong, D., & Grundahl, F. 2008, ApJL, 672, L29
Yong, D., Grundahl, F., D'Antona, F., et al. 2009, ApJL, 695, L62
Yong, D., Norris, J. E., Bessell, M. S., et al. 2013, ApJ, 762, 26
Yong, D., Roederer, I. U., Grundahl, F., et al. 2014, MNRAS, 441, 3396